Supporting Information

Covalently Sewing Dual-Sided Janus Coating via Photoiniferter Surface Chain Extension

Baoshan Hou, Chenyu Wu, Zipeng Zhang, Cuijuan Xuan, Chao Xing, Peng Xu*, Xiaonan Kan**

C. Xing, P. Xu

Department of Burns and Plastic Surgery, Department of Plastic and Reconstructive Surgery, Institute of Traumatic Medicine, Shanghai Ninth Hospital, Shanghai Jiao Tong University School of Medicine, Shanghai 200011, P. R. China.

E-mail: xingchao@sjtu.edu.cn, tomcat1975@sjtu.edu.cn

X. Kan

College of Polymer Science and Engineering, Qingdao University of Science and Technology, Qingdao 266042, P. R. China

E-mail: kanxn2011@iccas.ac.cn

B. Hou, C. Wu, Z. Zhang

Qingdao Institute for Theoretical and Computational Sciences, Center for Optics Research and Engineering, Shandong University, Qingdao 266237, P. R. China

C. Xuan

College of Chemistry and Pharmacy, Qingdao Agricultural University, Qingdao 266109, P. R. China

Table of contents

1. Materials S1
2. Instrumentation S2
3. Fabrication and Characterization of Janus coatings S12
   3.1 Optimization of the “adhesive layer” S12
   3.2 Optimization of the “hydrophobic layer” and “oleophobic layer” S19
   3.3 Fabrication of hydrophobic-hydrophilic gradient materials S27
   3.4 Characterization of the fabricated Janus double-layered coatings S30
   3.5 Mechanical properties of the as-prepared coatings for long-term anti-corrosion applications S33
4. Anti-corrosion performance of different coatings on AZ31B alloy S36
   4.1 Electrochemical testing analysis S36
   4.2 AZ31B protected from different coatings through neutral salt spray test S46
   4.3 Anti-corrosion performances of different coatings when immersed in 3.5% NaCl solution S49
   4.4 In-situ scanning vibration electrode (SVET) measurements S51
   4.5 Anti-corrosion performances of different coatings on Q235 mild steel and H62 brass S54

Supporting references S59

1. Materials

N,N'-dimethylacrylamide (DMA, 98%), *N,N*'-diethylacrylamide (DEA, 98%), 2-hydroxyethyl acrylate (HEA, 97%), butyl acrylate (BA, 99%) were sourced from Macklin. Phenyl acrylate (PA, 97%), pentafluorophenyl acrylate (PFPA, 98%), 2,2,2-Trifluoroethyl acrylate (TFEA, 98%), hexafluorobutyl acrylate (HFBA, 98%), 1H,1H,5H-octafluoropentyl acrylate (OFPA, 98%), 1,4-butanediol diacrylate (BDDA, 90%) 1H,1H-perfluorooctyl acrylate (PFOA, 98%), 3,3,4,4,5,5,6,6,7,7,8,8,8-tridecafluorooctyl acrylate (TFOA, 99.8%), 3-methyl-1H-indazole, 2,2'-azobis(2-methylbutyronitrile), n-hexadecane, dimethyl silicone oil (visibility 920-1800 mPa·s), vacuum pump oil were purchased from Bidepharm. KOH, I_2, $Na_2S_2O_3$, tetrahydrofuran, carbon disulfide, ethanol, ethyl ether, n-hexane were ordered from Sinopharm Chemical Reagent. 1H,1H,7H-dodecafluoroheptyl acrylate (DFHA, 98%) was ordered from Meryer (Shanghai) Biochemical Technology Co., Ltd. Rust-Oleum (RO) and Very High Temperature (VHT) coatings were purchased from Taobao Marketplace (Alibaba Group, Hangzhou, China).

The metal substrates used were AZ31B magnesium alloy (composition (wt%): Al 2.5-3.5, Si 0.08, Ca 0.04, Zn 0.6-1.4, Mn 0.2-1.0, Fe 0.003, Cu 0.01, Mg balance), Q235 mild steel (composition (wt%): C 0.17, Si 0.17, Mn 0.20, P 0.013, S 0.016, and Fe balance) and H62 brass alloy (composition (wt%): Cu 61.8, Fe 0.13, Pb 0.002, Sn 0.006, S 0.002, P 0.002, and Zn balance). Samples sized 10 mm × 10 mm × 3 mm were used as working electrodes for electrochemical tests, with the backside welded with a copper conductor and encapsulated with epoxy resin, exposing a working surface area of 1 cm^2.

Cylindrical specimens of Φ 20 mm × 3 mm were used for adhesion tensile tests, and samples of 40 mm × 13 mm × 2 mm were used for salt spray corrosion tests. Before the experiments, all sample working surfaces were sequentially polished with 200, 400, 600, 800, 1000 grit sandpaper, washed with ethanol and deionized water, and air-dried with cold air.

2. Instrumentation

The synthesis of bis(3-methyl-1H-indazole-1-carbothioic) disulfide [1, 2]: 3-Methyl-1H-indazole (1.32 g, 10 mmol) was added to a solution of potassium hydroxide (561 mg, 10 mmol) in tetrahydrofuran (50 mL) at 0-5 °C. The mixture was stirred at 0-5 °C for 15 min. Thereafter carbon disulfide (0.902 mL, 1.142 g, 15 mmol) was added slowly. The reaction mixture was stirred for 1 h at 0-5 °C. Subsequently, I_2 (2.54 g, 10 mmol) was added dropwise in excess, and the reaction was stirred continuously for 4-6 h before adding sodium thiosulfate ($Na_2S_2O_3$) (0.79 g 5 mmol) to neutralize the excess I_2. The yellow solids were extracted with ethyl ether, which was followed by the filtration. The obtained solution was washed 3 times with deionized water and then dried to get bis(3-methyl-1H-indazole-1-carbothioic) disulfide (1.81 g, 87% yield).

The synthesis of 2-cyanobutan-2-yl 3-methyl-1H-indazole-1-carbodithioate (InZ): A solution of bis(3-methyl-1H-indazole-1-carbothioic) disulfide (4.14 g, 10 mmol) and 2,2'-azobis (2-methylbutyronitrile) (3.69 g, 40 mmol) in ethyl acetate (150 ml) was heated at reflux for 12 hours under the nitrogen atmosphere. After the removal of the volatiles in vacuo, the crude product was subjected to column chromatography with ethyl acetate: n-hexane 1:12 as eluent. The product 2-cyanobutan-2-yl 3-methyl-*1H*-

indazole-1-carbodithioate was collected and dried to obtain 3.59 g yellow solid (62 % yield).

Preparation of Polymer Coating through Photo-Controlled RAFT: The general process for preparation of layered coating is as follows. First, different adhesion or hydrophobic/oleophobic monomers were placed in dark brown glass vials. According to the different monomer, cross-linker, and RAFT agent molar ratios, cross-linker (BDDA) and RAFT agent (InZ) were added, mixed uniformly by ultrasonication for 5 minutes. The mixed solution was then applied onto the pretreated metal substrate surface in an amount of 5 μL/cm^2, covered with a 0.15 mm thick FEP (Fluorinated ethylene propylene) release film to evenly spread the solution over the substrate surface. The substrate was then exposed to light from a 10 W LED source with a wavelength of 425 nm at a distance of 10 cm for 10 minutes to polymerize the monomers. This process was repeated on substrates with adhesive coatings to prepare multilayer adhesive/hydrophobic coatings. Moreover, for each layer, to achieve best performances, several kinds of monomers were screened, as summarized in Table S1. This geometry-controlled setup defines the coating thickness because the applied resin is confined by the fixed casting geometry (areal dosage + FEP spacer), which promotes uniform spreading and reproducibility when the same parameters are used. In principle, the cured thickness can be tuned by adjusting the resin dosage (μL cm^{-2}) and/or the spacer thickness, while keeping the irradiation conditions unchanged to ensure complete curing.

Chain extension experiments: The synthesis of the first block (polyDMA-macroRAFT)

was performed using a fixed reaction stoichiometry of [DMA]:[InZ] = 50:1, under 10 mW cm^{-2} 425 nm irradiation for 7 min in the presence of oxygen; chain extension was performed using a fixed reaction stoichiometry of [MA]:[polyDMA-macroRAFT] = 300:1, under 10 mW cm^{-2} 425 nm irradiation for 3 min in the presence of oxygen.

Nuclear Magnetic Resonance (NMR): NMR analysis was performed on a 400 MHz Bruker Advance NEO instrument installed with SampleXpress operating for ^{1}H with CDCl3 as solvent. Spectra were reported as chemical shift (δ, ppm) relative to tetramethylsilane (TMS).

Mass spectrometry (MS). MS test was conducted using a Thermo Scientific Q Exactive Focus instrument, utilizing atmospheric pressure ionization chemical (APIC) as the ion source and dichloromethane as the solvent.

Photopolymerization Setup: The polymerization solutions were irradiated at 10 mW cm^{-2} LED source with a wavelength of 425 nm at a distance of 10 cm at room temperature.

Fourier Transform Infrared (FTIR) spectroscopy: FTIR spectroscopy was performed by a Thermo Scientific Nicolet iS10 spectrophotometer.

Scanning electron microscope measurement (SEM): SEM image was obtained from SEM, JEOL JSM-6490, and EDX analysis was obtained from Energy Dispersive Spectroscopy (EDAX, Pegasus XM4).

Water and oil contact angle measurements: The water and oil contact angle measurements were performed using a POWEREACH JC2000DM instrument. For contact angle measurements, 2 μL water or oil sample was dispensed onto the specimen

surface through the automated injection device of the instrument. And a side-view image was captured using a high-speed charge coupled device (CCD) camera once the droplet stabilizes. The captured image was then analyzed automatically by testing software or manually through a five-point fitting method to accurately determine the water contact angle. All the data ware obtained from five measurements of five parallel samples.

Chain extension experiments and Size exclusion chromatography (SEC) tests: The synthesis of the first block (polyDMA-macroRAFT) was performed using a fixed reaction stoichiometry of [DMA]:[InZ] = 50:1, under 10 mW cm^{-2} 425 nm irradiation for 7 min in the presence of oxygen; chain extension was performed using a fixed reaction stoichiometry of [MA]:[polyDMA-macroRAFT] = 300:1, under 10 mW cm^{-2} 425 nm irradiation for 3 min in the presence of oxygen. SEC with DMF as eluent was used to characterize molecular weight distribution of polymers. The SEC modular system is composed of a Shodex (KD-G 4A) 8.0 μM bead size guard column followed by a Shodex (GPC-KD-803) 6.0 uM bead size columns, a differential refiractive-index detector, and a UV detector. The SEC system was calibrated based on narrow molecular weight distribution of poly(*N,N'*-dimethylacrylamide) standards with molecular weights of 1000 to 50000 g mol^{-1}.

Tensile performance and pull-off adhesion tests: The tests were conducted using the SUNS UTM6104X universal testing machine. The tensile test specimen was prepared according to the 1BA type described in ISO 527-2-2019. The specimen was secured in the testing machine, and a tensile force was applied at a rate of 1 mm/min until the

specimen fractured, in accordance with the ISO 527-2-2019 standard. The adhesion of coatings was determined using pull-off test method according to ISO 4624-2016. First, two 20 mm diameter dollies (test fixture) were adhered to the both sides of the coated specimen, then, a perpendicular force was applied through a tensile testing machine at a rate of 1 mm/min until the dolly and coating detach from the substrate.

Pencil hardness test: The coating hardness was measured with an Aipli QHQ-A pencil hardness tester. In accordance with the ISO 15184-2020 standard, the pencil hardness test was conducted to ascertain the hardness of the coating. Pencils of varying hardness levels were drawn across the surface of the coating at a 45-degree angle under a load of 750 g. The hardness level of the pencil that did not mar the coating surface can be considered as coating hardness.

Cross-cut test: The cross-cut test serves as a qualitative, visual method for assessing the adhesion of coatings. Utilizing an Aipli QFH-A type six-bladed tool with a blade spacing of 1 mm, a lattice pattern of incisions was made on the coating surface, penetrating through the coating to reach the substrate. Subsequently, Scotch 600 adhesive tape was employed to remove any loosened coating. The extent of coating removal was evaluated and rated according to the criteria set forth in ISO 2409-2020, thereby quantifying the coating's adhesive performance.

Bending test: The coating bending tests were conducted using a QTY-32 paint film cylindrical bending instrument, in accordance with the ISO 1519-2022 standard. The coated specimen was positioned back-side against the cylindrical mandrel and firmly secured. Subsequently, the specimen was bent 180° around the mandrel by a spiral

handle. During this process, the coating was meticulously observed for the emergence of cracks or detachment from the substrate, thereby providing a measure of the coating's flexibility and adherence properties under stress. In the test, the diameter of the mandrel was progressively reduced from 15mm to 0.5mm.

Corrosion Electrochemical Test: Electrochemical tests were evaluated using a Corrtest CS310X electrochemical workstation in 3.5 wt% NaCl aqueous solution. Uncoated or coated AZ31B, Q235 or H62 served as the working electrode, with a Pt sheet as the counter electrode and a saturated calomel electrode (SCE) as the reference electrode. Corrosion monitoring over 30 days was conducted using methods such as open circuit potential (OCP), electrochemical impedance spectroscopy (EIS), and linear polarization resistance (LPR), with potentiodynamic polarization curves (PDPC) tests performed at the end of the experiment. EIS tests were performed at a frequency range from 100 kHz to 0.01 Hz and a perturbation of 5 mV versus OCP. LPR was performed in a potential range of ± 10 mV vs. OCP with a scanning rate of 0.066 mV/s. PDPC was performed in a potential range of ± 250 mV vs. OCP with a scanning rate of 0.5 mV/s.

Salt Spray Corrosion Test: Samples backsides and edges were sealed with epoxy resin, with the bare or coated front serving as the working face. According to ISO 9227-2022 standard, a neutral salt spray test (NSS) was conducted in a ZLHS-90-SH 270L salt spray test chamber using a pH 6.5-7.2, 5 % NaCl solution with an average collection rate of 1.8-2.2 ml/h at a temperature of 35 °C for 24 hours. Each experiment was conducted in duplicate. After the salt spray corrosion test, the samples were carefully

rinsed and dried. The corrosion assessment of the samples was conducted through visual inspection, SEM and EDX analysis.

Scanning vibration electrode (SVET) measurements: SVET measurements utilized a Uniscan M370 scanning electrochemical workstation, equipped with a 10 μm diameter Pt-Ir microprobe coated with platinum black. The probe was positioned approximately 100 μm above the coating surface and vibrated with a 30 μm amplitude along the Z direction (perpendicular to the surface). In addition, scanning was conducted across a 2000 μm × 2000 μm area on the sample surface with a step size of 25 μm. The distribution of current density j (μA/cm^2) can be determined from the distribution of potential difference $\Delta\varphi$ (V) along the X and Y axes obtained through SVET measurements [3]:

$$j = -\Delta\varphi\frac{k}{d}$$

where k is the conductivity of the 3.5 % NaCl solution, which is 5.6 × 10^4 μS/cm, and d is the vibration amplitude 3.0 × 10^{-3} cm.

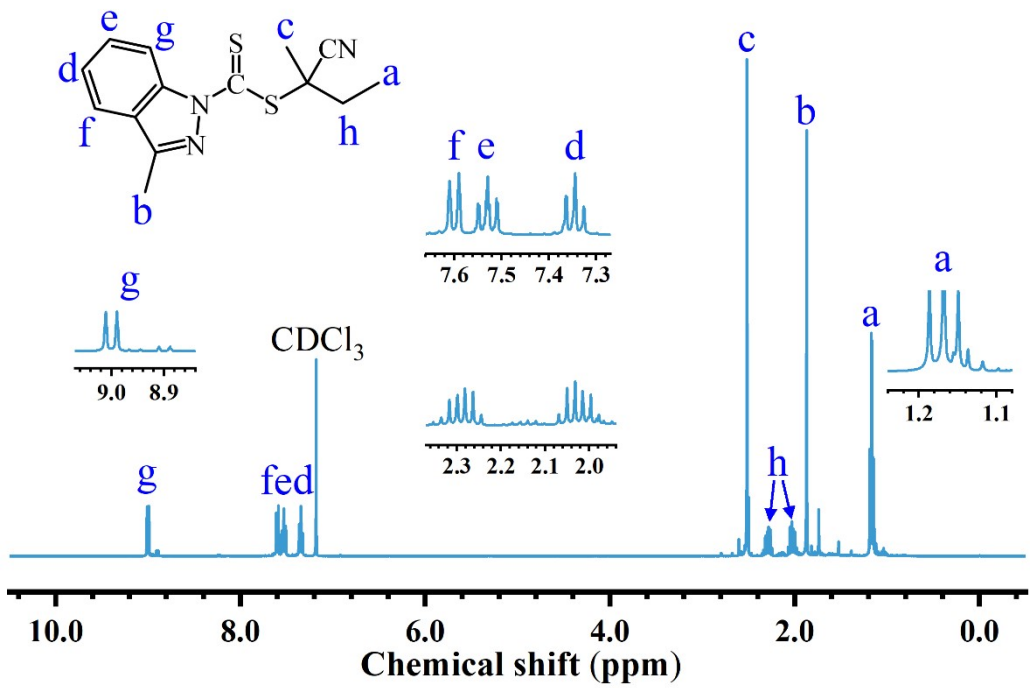

Figure S1. ^{1}H-NMR spectroscopy of InZ.

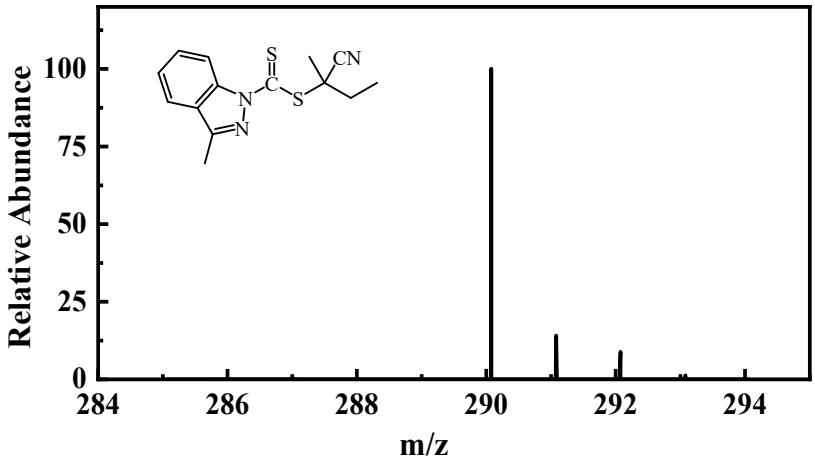

Figure S2. Mass spectrum of InZ.

In the mass spectrum, the most intense ion peak at m/z 290.08 was observed, which represented the molecular ion peak of InZ. The subsequent peaks at m/z 291.08 and 292.07 can be attributed to $[InZ+H]^+$, $[InZ+2H]^+$.

Table S1. Monomers for adhesive layer and hydrophobic/oleophobic layer.

Adhesive monomer	**DMA**	**DEA**	**HEA**	**PA**	**PFPA**
Name	N,N-Dimethylacrylamide	N,N-Diethylacrylamide	2-Hydroxyethyl acrylate	Phenyl acrylate	Pentafluorophenyl acrylate
Structure	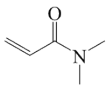	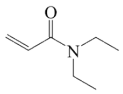	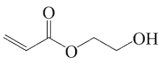	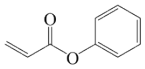	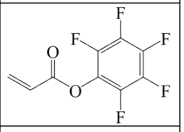
Molecular weight (g/mol)	99.13	127.18	116.12	148.16	238.11

Hydrophobic monomer	**BA**	**TFEA**	**HFBA**	**OFPA**
Name	Butyl acrylate	2,2,2-Trifluoroethyl acrylate	Hexafluorobutyl acrylate	1H,1H,5H-Octafluoropentyl acrylate
Structure	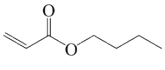	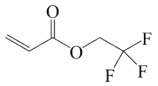	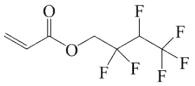	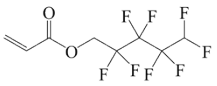
Molecular weight (g/mol)	128.17	154.02	236.11	286.12

Oleophobic monomer	**PFOA**	**TFOA**	**DFHA**
Name	1H,1H-Perfluorooctyl acrylate	3,3,4,4,5,5,6,6,7,7,8,8,8-Tridecafluorooctyl acrylate	1H,1H,7H-Dodecafluoroheptyl acrylate
Structure	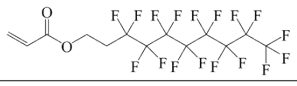	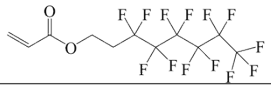	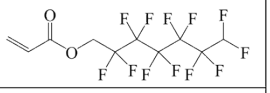
Molecular weight (g/mol)	518.17	418.15	386.14

3. Fabrication and Characterization of Janus coatings

3.1 Optimization of the “adhesive layer”

For “adhesive layer”, a model system was initially tested using N,N-Dimethylacrylamide (DMA) as monomer, by regulating molar ratios of [DMA]/[BDDA]/[InZ], the adhesive force changed accordingly. As can be seen from Figure S3 and Table S2, maximum adhesive force can be realized when the molar ratio of [DMA]/[BDDA]/[InZ] was 200:5:1. Based on these results, the molar ratio was fixed at 200:5:1 in the following experiments. In addition, for all the monomers tested here, pentafluorophenyl acrylate (PFPA) showed largest adhesive force, reaching an average of 13.3 Mpa. To further check the stability of the adhesive layer, a series of tests were performed following the international standards, for instance, pencil hardness test (ISO 15184-2020), cross-cut test (ISO 2409-2020), pull-off test for adhesion (ISO 4624-2016) etc. (Table S3). Interestingly, among all the test results, PFPA showed the best performance and was chosen as monomer for the adhesive layer (Figure S4, S5). Besides, another important character of adhesive layer is resistant to water impalement, consequently, all prepared layers were immersed in water to evaluate the subsequent water absortion rate. As can be seen, layers made from PFPA showed nearly zero absorbtion of water over long period (144 h, Figure S6), which can be attributed to its intrinsic property of low surface energy, covering by fluoride.

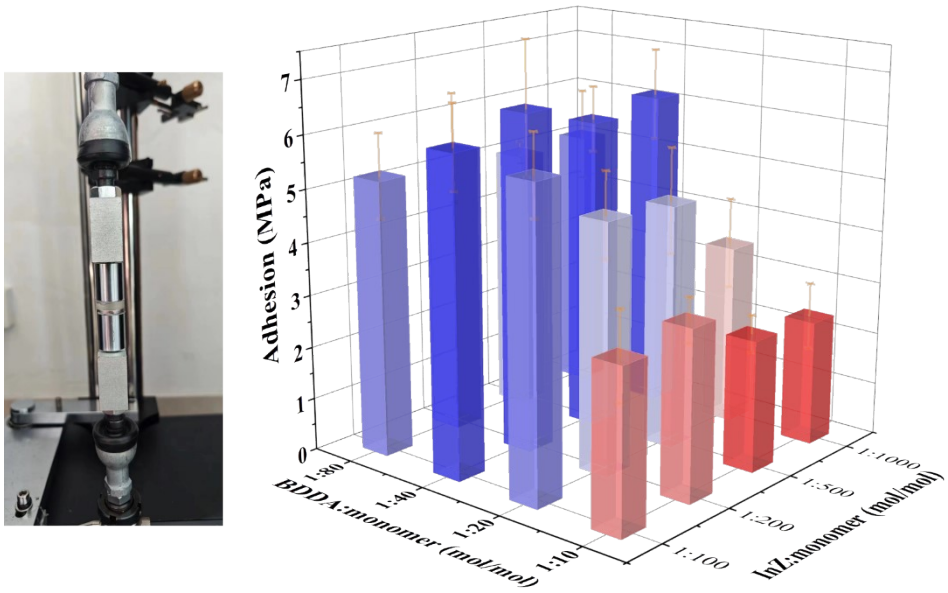

Figure S3. Adhesion measurement by using DMA as model monomer for adhesive coating with different molar ratio of [DMA]/[BDDA]/[InZ].

Table S2. Detailed data of adhesion measurement when DMA as model monomer for adhesive coating with different molar ratio of [DMA]/[BDDA]/[InZ].

BDDA: DMA	InZ: DMA	Adhesion (MPa)					Average adhesion (MPa)	Standard deviation (MPa)
1:80	1:100	6.2	4.0	5.2	5.2	5.5	5.2	0.8
	1:200	4.1	5.0	5.9	5.2	6.9	5.4	1.0
	1:500	5.3	4.9	5.2	4.9	4.8	5.0	0.2
	1:1000	5.7	3.9	4.9	6.2	4.7	5.1	0.9
1:40	1:100	7.1	6.5	5.6	5.1	5.8	6.0	0.8
	1:200	7.5	5.6	5.1	5.9	8.0	6.4	1.3
	1:500	5.7	5.2	5.9	6.0	6.9	5.9	0.6
	1:1000	7.6	5.3	5.9	6.2	5.7	6.1	0.9
1:20	1:100	4.9	5.3	6.2	5.9	6.8	5.8	0.7
	1:200	4.8	5.2	5.8	4.3	3.7	4.8	0.8
	1:500	5.9	4.1	5.6	3.9	3.8	4.7	1.0
	1:1000	2.8	4.5	2.6	3.1	4.3	3.5	0.9
1:10	1:100	3.7	2.8	2.6	2.1	4.1	3.1	0.8
	1:200	3.7	3.6	3.1	3.0	2.7	3.2	0.4
	1:500	2.5	2.4	3.1	2.3	2.2	2.5	0.4
	1:1000	2.5	3.1	1.5	2.0	2.8	2.4	0.6

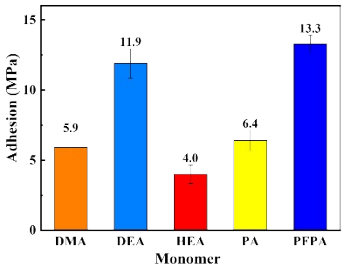

Monomer	Adhesion force (Mpa)					Avg (MPa)
DMA	5.3	6.6	5.5	7.2	5.1	6.0
DEA	13.0	12.1	11.2	10.5	12.7	11.9
HEA	4.0	4.9	3.9	4.3	3.1	4.1
PA	5.2	7.2	6.3	6.5	6.6	6.4
PFPA	14.1	12.9	12.9	13.7	12.7	13.3

Figure S4. Adhesion measurement of different monomers used for fabrication of adhesive layer with molar ratio fixed at [Monomer]/[BDDA]/[InZ] = 200:5:1.

Table S3. Mechanical strength of adhesive layers fabricated from different monomers.

Monomer	Pencil hardness test	Scribe test	Bend test
DMA	2B	5/4/5	< 0.5 mm
DEA	2B	4/4/5	< 0.5 mm
HEA	2B	2/0/1	< 0.5 mm
PA	H	0/1/1	2 mm
PFPA	B	0/0/0	< 0.5 mm

a)

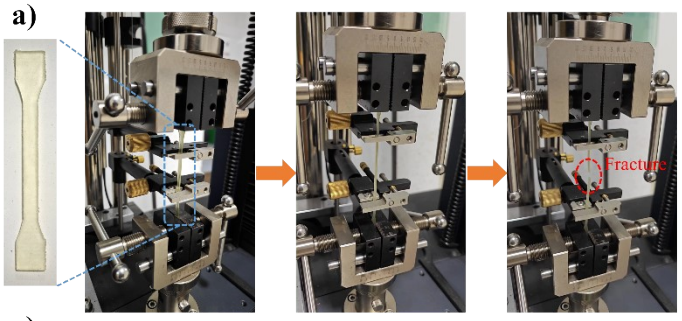

b)

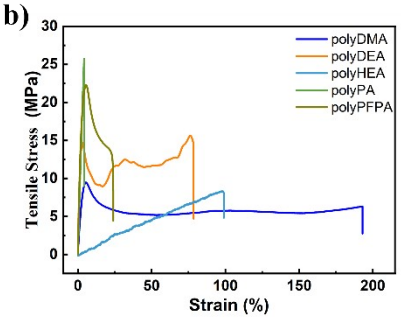

c)

Adhesive layer	Tensile strength (MPa)	Elongation at break (%)
polyDMA	9.5	193.0
polyDEA	15.7	78.4
polyHEA	8.3	50.6
polyPA	25.8	4.2
polyPFPA	22.3	24.0

Figure S5. Tensile behavior of different adhesive layers. a) Tensile test sample and setup; b) Tensile curves and c) detailed data of different adhesive layers.

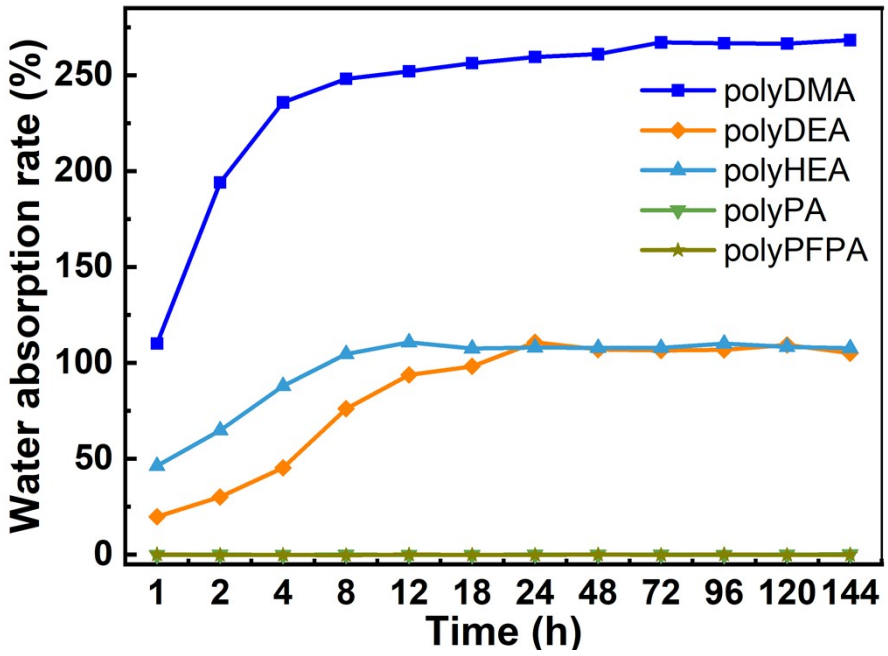

Figure S6. Water absorption rate of adhesive layer fabricated from different monomers.

3.2 Optimization of the “hydrophobic layer” and “oleophobic layer”

For hydrophobic layer, butyl acrylate (BA) and several fluorinated acrylates were used as test monomers. Water contact angle (WCA) was firstly measured of the polymerized products. As anticipated, fluorinated acrylates all showed better hydrophobicity owing to reduced surface energy compared with BA (Figure S7). Among them, 1H,1H,5H-Octafluoropentyl acrylate (OFPA) layer showed highest water repellency thanks to higher degree of fluorination with WCA reaching 114°. By simply drop-coating a solution of mixture containing OFPA, BDDA and InZ onto the as-prepared adhesive layer, the mixture can be cross-linked and polymerized under illumination of light, forming the second hydrophobic layer. The adhesive force of the composite coating with different constitutes was measured, and when employing OFPA for construction of second layer, maximum average adhesive force can be realized (9.0 MPa) (Figure S9). Therefore, a combination of PFPA and OFPA was chosen in the following experiments. The composite coating was robust enough thanks to the covalent connection between two separate layers. Furthermore, for better incorporation with adhesive layer, the molar ratio of [OFPA]/[BDDA]/[InZ] was optimized and fixed at 200:40:1.

For oleophobic layer, the composition of the oleophobic layer is oleophobic monomer:BDDA = 200:40:1, with PFOA, TFOA, or DFHA selected as the oleophobic monomer. The oleophobic layer material is applied to the surface of the adhesive layer, at a dosage of 5 μL/cm². The substrate is then exposed to a 10 W LED light source with a wavelength of 425 nm at a distance of 10 cm for 10 minutes to polymerize the

monomers, thus forming the multilayer oleophobic coating. Oil contact angle (OCA) was measured using several common oils, namely, n-hexadecane, silicon oil and vacuum pump oil (Figure S8). As expected, the as-prepared polyPFOA exhibited the highest apparent contact angles greater than 90° for all tested oils, reaching 107°, 100°, and 105°, respectively. While polyTFOA showed moderate oleophobicity, with OCA reaching about 90°. In contrast, polyDFHA showed oleophilicity, the OCA for n-hexadecane, silicon oil and vacuum pump oil was 54°, 52° and 55°, respectively. In consequence, polyPFOA was chosen as oleophobic layer for the following experiments. These results clearly indicates that the prepared coating has good potential for hydrophobic and oleophobic applications. Furthermore, these results cohesively demonstrated the universality of our strategy in fabricating various surfaces with different wettability.

For the abrasion tests via sandpaper, the graph included in the image indicates the WCA of the coating as a function of the abrasion cycles. Initially, the coating displays a WCA of 114°, indicative of its hydrophobic nature. After 20 cycles of abrasion, a slight increase in the WCA to 116° is observed, showcasing the coating's remarkable ability to maintain its hydrophobicity under mechanical stress (**Figure 1b**, Figure S10). This slight increase could be attributed to the microstructural rearrangement of the coating's surface, which can sometimes lead to an increase in hydrophobicity when certain roughness features become more pronounced or when lower energy surfaces are exposed. The stability of the WCA suggests that the coating's hydrophobic properties remains largely unaffected by the abrasion. For comparison, hydrophobic coating made

from OFPA was tested under the same condition. The polyOFPA alone was not resistant to the abrasion, as can be seen from Figure S11, the WCA declines dramatically with increasement of abrasion cycles and the film will break after only 10 cycles of abrasion. This result demonstrates the coating's resilience and potential for long-term applications, which can be attributed to the strong support of the adhesive layer here benefiting from highly covalently connected structures.

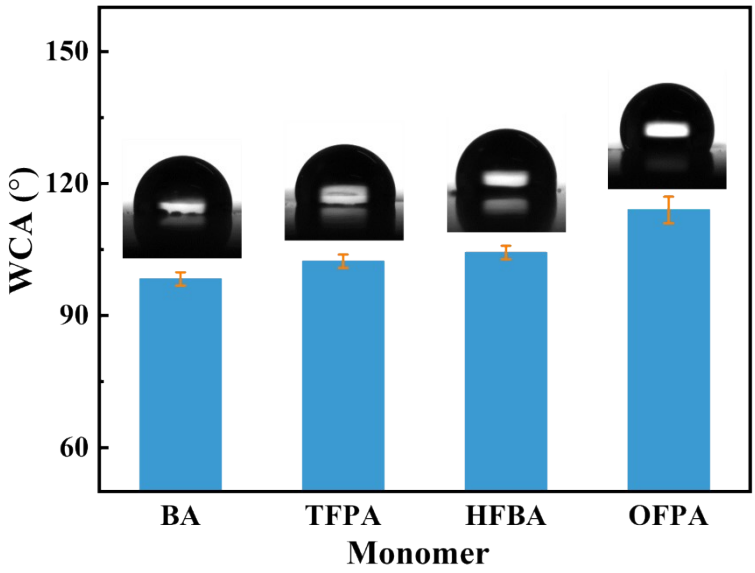

Figure S7. Water contact angle (WCA) measured of layers fabricated from different monomers.

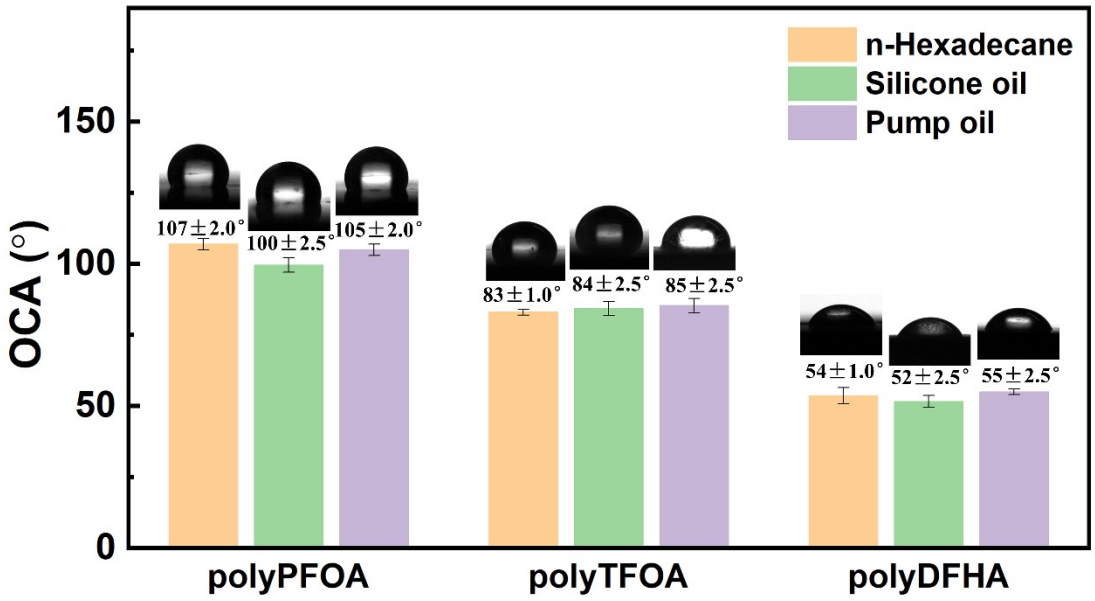

Figure S8. Oil contact angles (OCAs) of polyPFOA, polyTFOA and polyDFHA tested with three different kinds of oils, namely, n-hexadecane, silicon oil and vacuum pump oil.

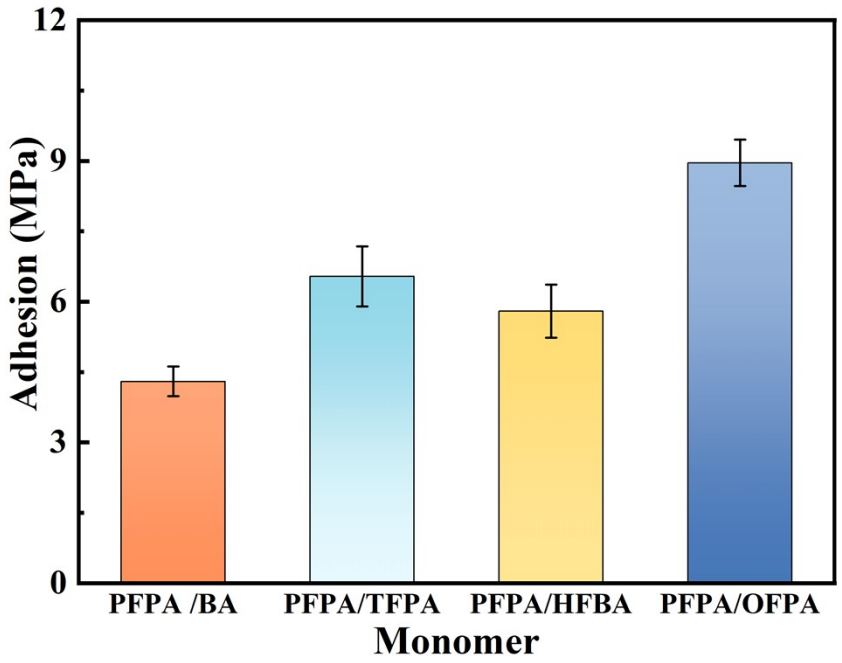

Figure S9. Adhesion strength across formulations of different monomers for hydrophobic layer.

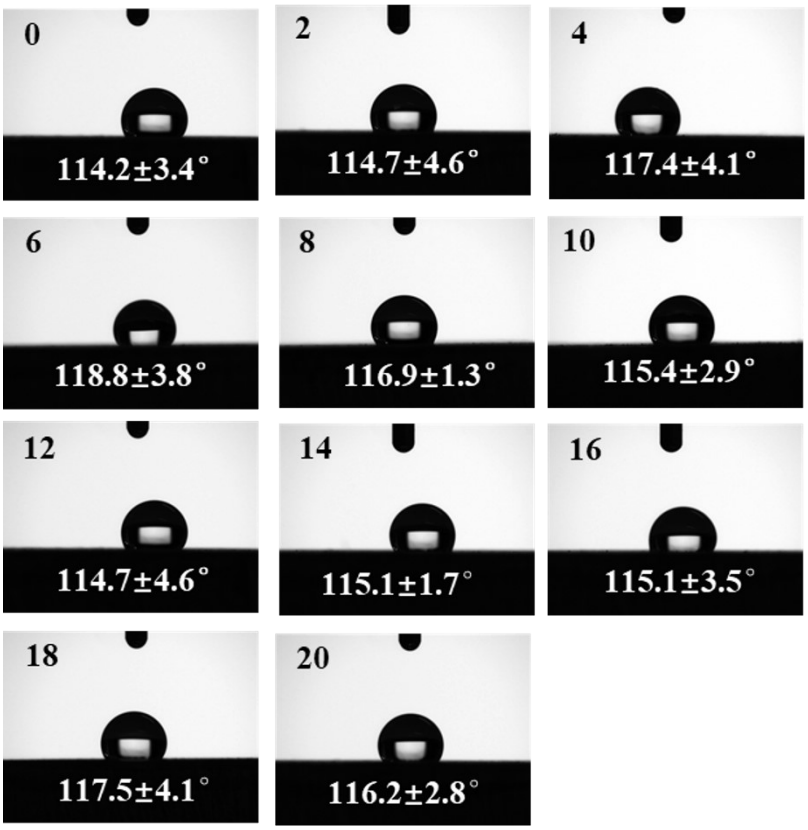

Figure S10. Photographs of WCAs of polyPFPA/polyOFPA undergoing every two wear cycles via sandpaper abrasion.

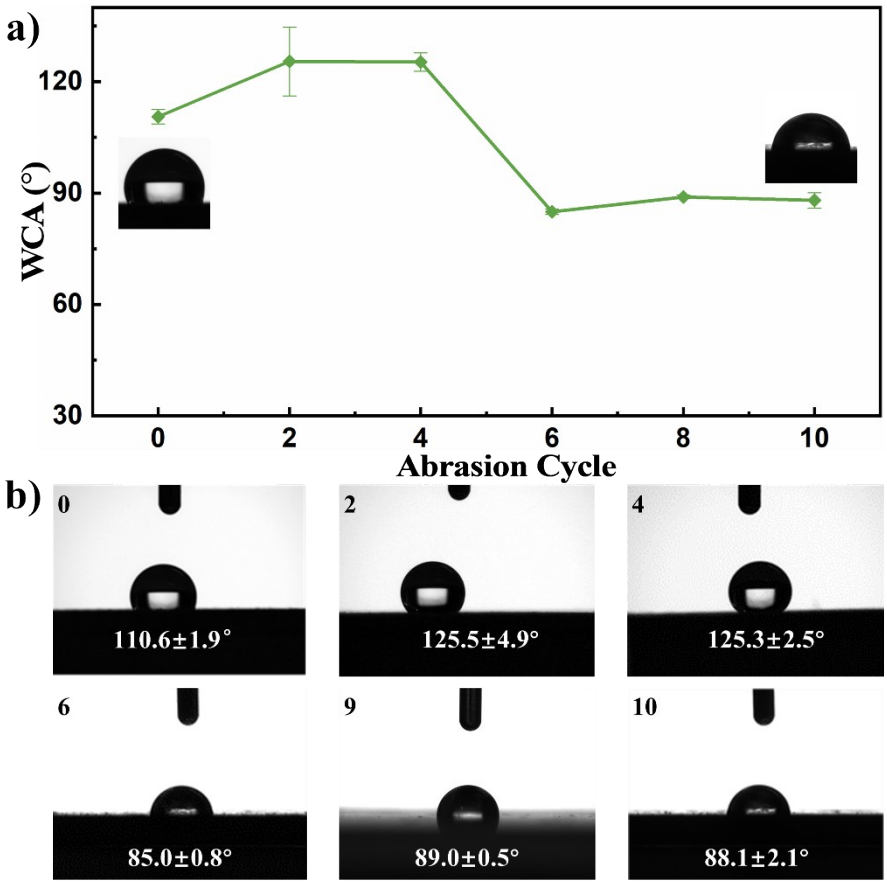

Figure S11. a) Wear resistance via sandpaper abrasion and WCAs of coatings fabricated from polyOFPA only. b) Photographs of WCAs of polyOFPA undergoing every two wear cycles via sandpaper abrasion.

3.3 Fabrication of hydrophobic-hydrophilic gradient materials

According to the molar ratios of each ingredient listed in the Table S4, prepare four solutions sequentially in the brown small bottle, and mixed uniformly by ultrasonication. Transfer 200 μL of the prepared solution for the first layer into a 10 mm × 10 mm × 10 mm silastic mold, and exposed to a 425 nm LED light source for polymerization. Then, use the same preparation method to sequentially fabricate the remaining layers on top of the first hydrophobic layer (with a solution dosage of 100 μL, 200 μL, and 200 μL for the second, third, and fourth layers, respectively), to obtain a gradient material that gradually transition from hydrophobicity on one side to hydrophilicity on the other side.

A 1 μL droplet of deionized water was placed on the sample surface, and the movement behavior was recorded by a CCD camera (Figure S12). As can be seen, when the water droplet is in contact with the surface of as-prepared gradient materials, it can spread along the wettability gradient immediately. This controlled unidirectional spreading behavior provided further evidence for the validity and controllability of our photo-RAFT strategy.

Table S4. Molar ratios of different monomers used in fabrication of gradient materials.

Layer	Thickness (mm)	PFOA	DEA	DMA	BDDA	InZ
1	2	200	0	0	40	1
2	1	60	140	0	15.5	1
3	2	0	200	0	5	1
4	2	0	0	200	5	1

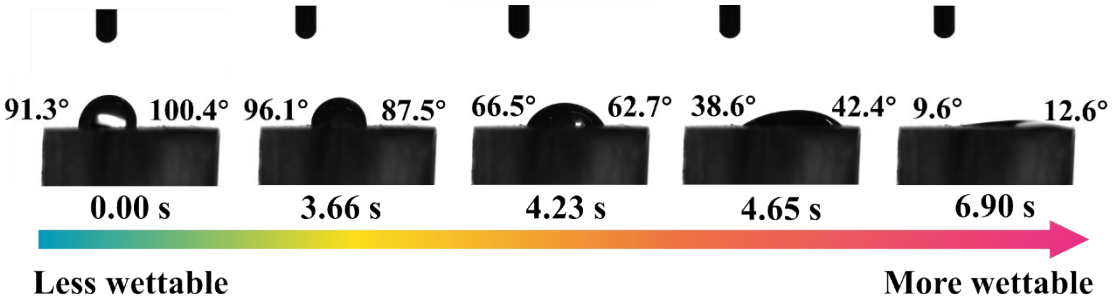

Figure S12. Photograph showing the change of WCAs along the gradient surface. The photograph was combined from five continuous photographs along the substrate captured at different time. The volume of the water droplets was kept at 1 μL.

3.4 Characterization of the fabricated Janus double-layered coatings

As shown in **Figure 2a**, the morphology of both layer is relatively flat and smooth thanks to the high cross-linking efficiency of RAFT polymerization. Besides, clear and continuous interface can be found without cracks or defects between two layers, demonstrating the layer was well connected with each other. To further verify successful fabrication of each layer, phenyl acrylate (PA) was chosen as the monomer for top layer. As shown in Energy Dispersive X-ray Spectroscopy (EDX) mapping in Figure S13, fluorine can only be found in the adhesive PFPA layer, confirming the successful fabrication of both layers and the composite film. Moreover, for the characterization of oleophobic layers, as indicated by Fourier-transform infrared analysis, polyPFOA, polyTFOA and polyDFHA coatings all exhibit broad absorption peaks at around 2960 cm^{-1}, corresponding to the stretching vibration of C-H of alkanes in the main or side chains. The absorption peaks between 1750-1730 cm^{-1} in the spectra of the three coatings are a hallmark of the acrylate carbonyl stretch. The fluorinated alkyl chain of the three polymers contributes to a series of peaks in the 1230-1110 cm^{-1} range, corresponding to its numerous -C-F- bonds (Figure S14).

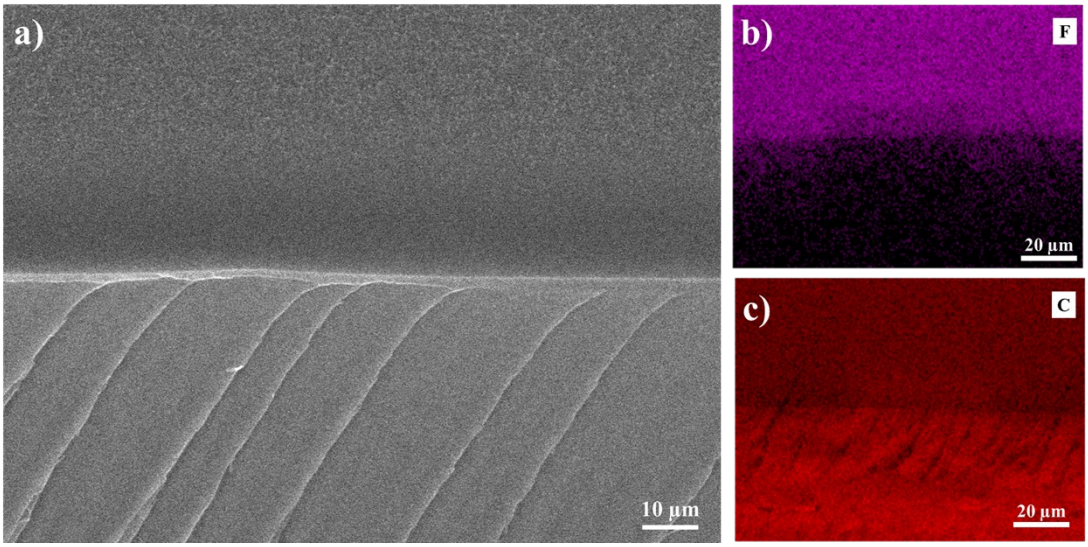

Figure S13. a) Cross-sectional SEM image of polyPA/polyPFPA double-layered coatings. The smooth top layer is the polyPFPA-based coating and the bottom layer refers to polyPA adhesive layer. b, c) EDX elemental mappings of C and F of the composite layer.

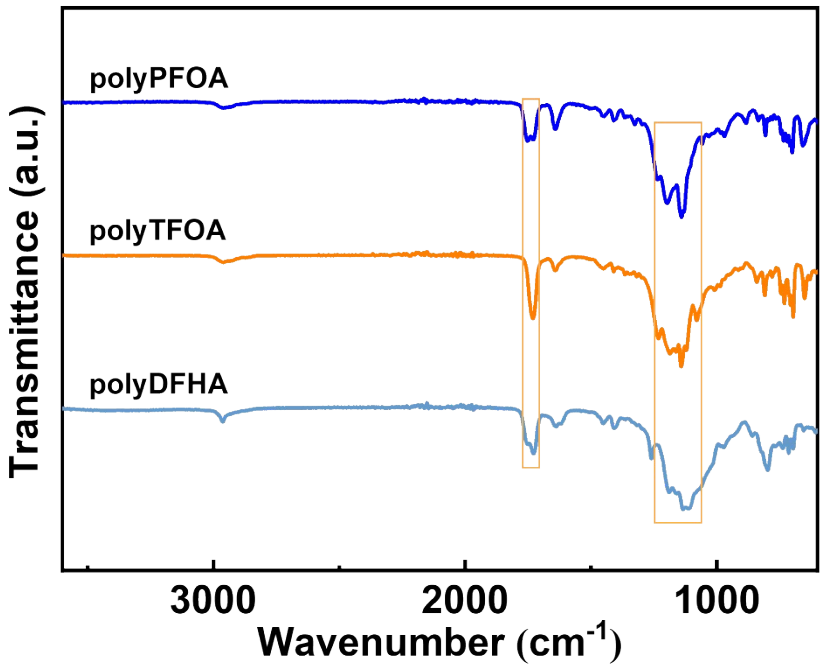

Figure S14. FT-IR analysis of oleophobic layers.

3.5 Mechanical properties of the as-prepared coatings for long-term anti-corrosion applications

To check the strength of covalent connection between different layers, hydrophilic-hydrophobic two-phasic tensile test specimens were prepared accordingly. The composition of the hydrophilic phase raw material was PFPA:BDDA = 200:5:1, while the hydrophobic phase raw material consisted of OFPA:BDDA = 200:40:1. First, the hydrophilic phase raw material was injected into a 1BA-type mold compliant with the ISO 527-2-2019 standard, and cured under a 425 nm light source. After curing, the sample was then cut in half using a knife. One half of the sample was placed back into the mold, while the remaining half of the mold was filled with the hydrophobic phase raw material. The sample was then cured under the 425 nm light source to obtain the hydrophilic-hydrophobic biphasic tensile sample (**Figure 2d**). Weights with different quality was added to test the bearing capacity of the sample. As can be seen, the as-prepared sample can hold weights to as heavy as 500 g, demonstrating the high strength of the formed covalent bonds between different layers.

The as-prepared Janus double-layered coatings have shown excellent mechanical properties, especially the adhesion between different layers due to the covalent connection endowed by photo-RAFT polymerization. For comparison, the adhesion strength of polyPFPA/polyOFPA and two commercial coatings, RO and VHT was measured. As shown in Figure S15, the adhesion strength both to metal surfaces and between polyPFPA and polyOFPA can be as large as 9.0 Mpa, while those for RO and

VHT were around 3.0 Mpa. The strong adhesion between different layers of our method is one of the vital prerequisite for long-term anti-corrosion applications.

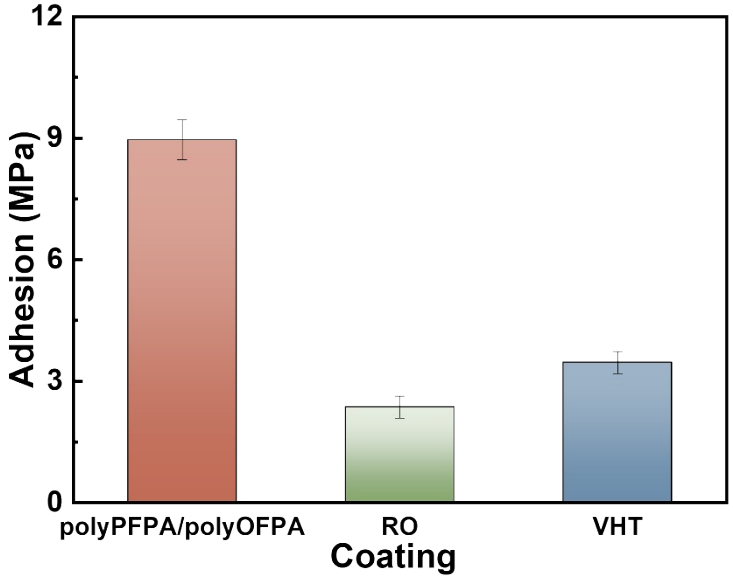

Figure S15. Comparison of adhesion strength of double-layered polyPFPA/polyOFPA coatings fabricated through RAFT and two commercial coatings, RO and VHT.

4. Anti-corrosion performance of different coatings on AZ31B alloy

4.1 Electrochemical testing analysis

In the equivalent circuits (Figure S16), R_s represents solution resistance, R_{ct} signifies the charge transfer resistance and CPE_{dl} is the constant phase element (*CPE*) representing the double layer capacitance. Additionally, R_f and CPE_f correspond to the resistance and *CPE* of coating film respectively. The circuit elements also include *L* for inductance, and the indicative of the inductive resistance R_L. In the EIS plots presented in Figure S16, the capacitive loop in the Nyquist plot manifests an extended loop deviating from the ideal semicircle, due to the "dispersion effect" with the inhomogeneous surface Consequently, the capacitance is presented by *CPE* component. Figure S17 is an extension of **Figure 3h**, describing the EIS variation patterns for AZ31B with and without different coatings over various corrosion durations. The data fitting of these EIS curves was based on the equivalent circuits shown in Figure S16. And Table S5 lists the corresponding electrochemical parameters obtained by fitting the EIS curves.

As can be observed from Figure S17a-b, the EIS plots of bare AZ31B exhibit characteristics combining a capacitive reactance loop along with an inductive reactance loop. The formation of inductance may be attributed to dynamic changes in current distribution, which are in turn caused by dynamic changes in the electrode surface state during the rapid corrosion process. The EIS of bare AZ31B can be fitted with the equivalent circuit shown in Figure S16a, and the polarization resistance R_p can be calculated from R_{ct} and R_L [4]:

$$Rp = \frac{1}{\frac{1}{Rct} + \frac{1}{RL}}$$

The characteristics of the EIS curves and the smaller values of R_p (magnitude of 10^2) both indicate the rapid corrosion behavior of bare AZ31B in saline solution.

In addition, for AZ31B endowed with a PFPA layer (Figure S17c-d) during the initial corrosion phase (0~3 days), as well as throughout all phases of the polyOFPA layer (Figure S17e-f), the electrochemical impedance spectroscopy (EIS) distinctly manifests dual capacitive reactance loops. Within these electrochemical reaction regimes, the bifurcated time constants are distinctly attributable to the contributions from the electrical double layer and the coating layer, respectively. The EIS curves are amenable to fitting via the equivalent circuit depicted in Figure S16b, and the polarization resistance R_p can be calculated from R_f and R_{ct} [5]:

$$Rp = Rf + Rct$$

During the advanced stage (7~14 days) of the AZ31B coated with the polyPFPA layer, the characteristics of the EIS curves align with those of the uncoated AZ31B, signifying the failure of the polyPFPA layer. Consequently, the equivalent circuit utilized for analysis corresponds to that depicted in Figure S16b. The characteristics of the EIS curves in Figure S17c-f and the progressively decreasing R_p over time both indicate that a single layer of PFPA or OFPA cannot provide sufficiently stable corrosion resistance.

The EIS curves of AZ31B with polyPFPA/polyOFPA coatings (Figure S17g-h) exhibit the characteristic of a single time constant, due to the film capacitance (R_f) and

film resistance (CPE_f) in the electrode reaction. Therefore, the EIS plots were fitted using the equivalent circuit shown in Figure S16c, and $R_p = R_f$ [6]. This characteristic suggests that the coating possesses a very high impedance, indicative of its ability to isolate the substrate from the corrosive medium. Negligible R_{ct} and extremely high R_f ($>10^{10}$) suggest that the double-layer coating has an excellent ability to isolate the substrate from the corrosive medium.

Additionally, Figure S18 showed corrosion current density (I_{corr}) over time obtained from Linear Polarization Resistance (LPR) tests.

The I_{corr} is obtained from the Stern-Geary formula[7]:

$$I_{corr} = \frac{B}{R_p}$$

where B is the Stern-Geary coefficient, which can be obtained from the Tafel coefficients (b_a and b_c) of the anode and cathode in the polarization curve.

$$B = \frac{b_a b_c}{2.303\,(b_a + b_c)}$$

E_{corr} represents the corrosion potential. R_p is the polarization resistance, which is the slope of the linear polarization curves at E_{corr}:

$$R_p = \left[\frac{dE}{dI}\right]_{E_{corr}}$$

Compared to bare AZ31B, the application of polyPFPA/polyOFPA double-layer coatings led to a significant positive shift of E_{corr} (from -1.41V to -0.10V), as well as a notable reduction in I_{corr} and corrosion rate, all of which indicate the excellent corrosion resistance of the double-layer coatings. Correspondingly, for AZ31B coated with a

single layer of polyPFPA or polyOFPA, E_{corr} is close to that of bare AZ31B, with I_{corr} and corrosion rate slightly reduced, indicating that the single-layer coatings can only provide a relatively limited corrosion resistance capability.

Besides, Open circuit potential (OCP) stability of different layers over a month further demonstrated the best defense of Janus polyPFPA/polyOFPA against corrosion on AZ31B (Figure S19). Tafel extrapolation fitting was performed on the polarization curves within the overpotential range of 100~110 mV for both cathodic and anodic segments, and the fitted data are listed in Table S6.

All above electrochemical results indicate that the excellent corrosion protection performance of the double-layer coating prepared via RAFT polymerization is not merely a simple superposition of two single-layer coatings, but rather the result of both layers fully leveraging their strengths in a synergistic enhancement.

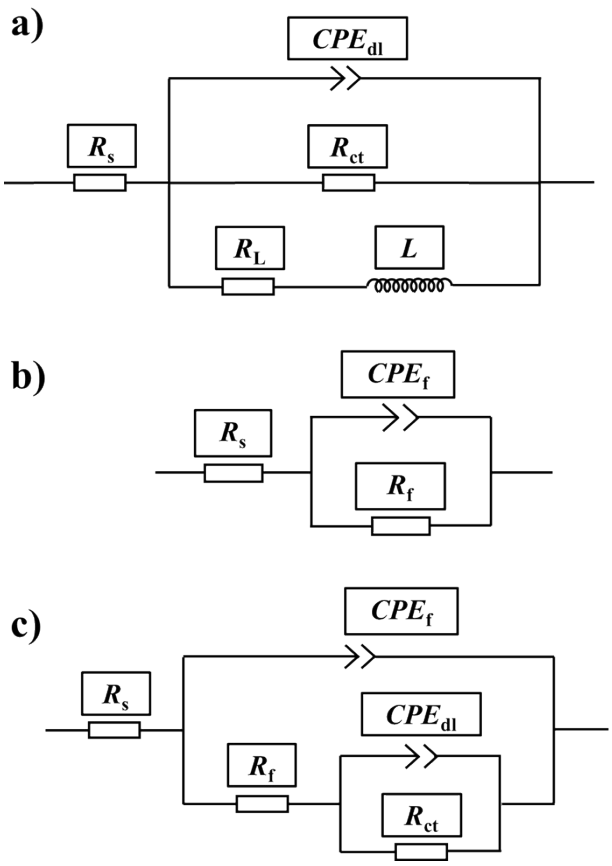

Figure S16. Equivalent circuit models for EIS analysis, a) with an inductive loop, b) with a single time constant and c) with dual time constants.

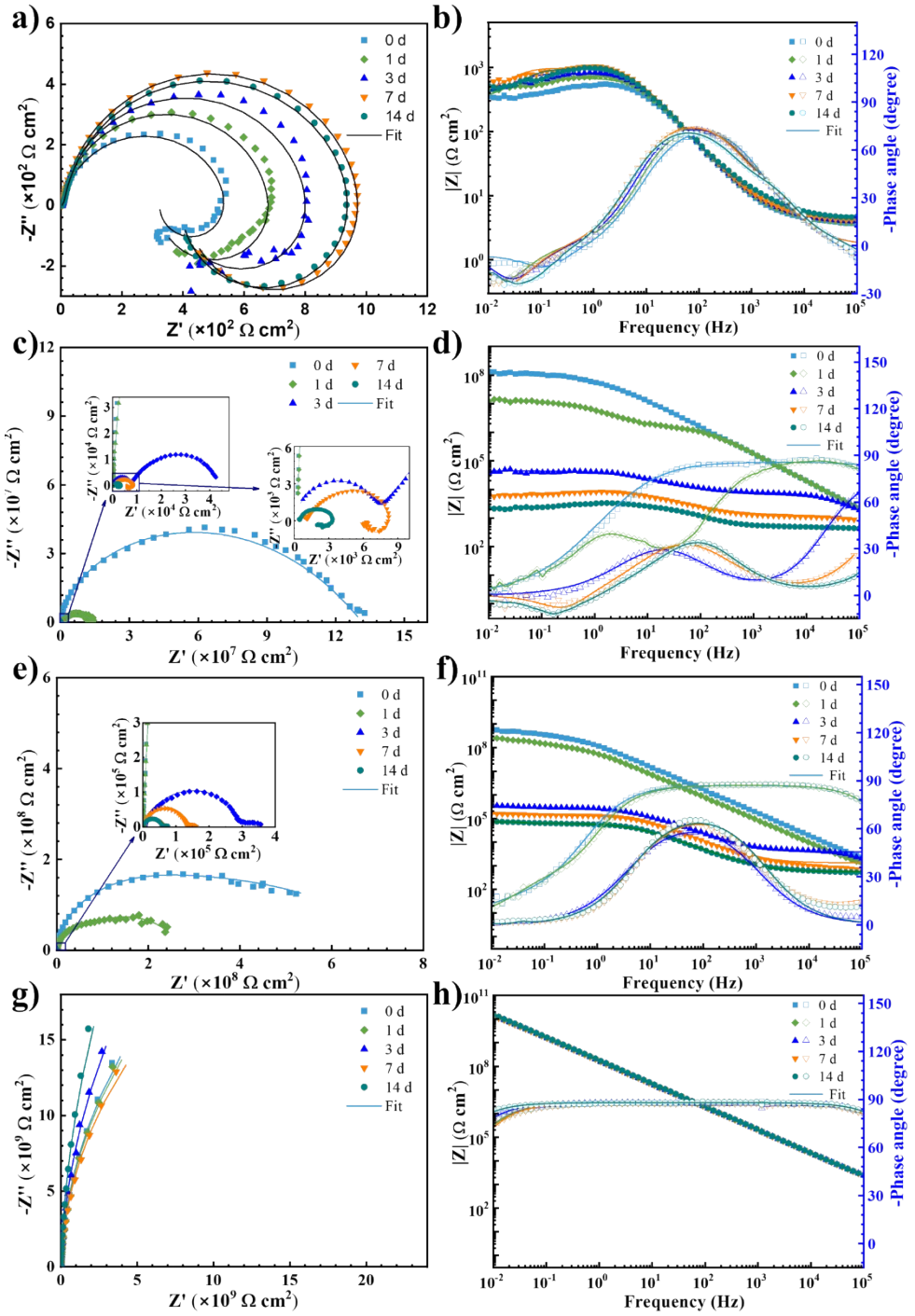

Figure S17. EIS of AZ31B Mg alloy with different coatings and different immersion corrosion times. Nyquist plots of a) bare AZ31B, c) polyPFPA@AZ31B, e) polyOFPA@AZ31B and g) polyPFPA/polyOFPA@AZ31B. Bode plots of b) bare AZ31B, d) polyPFPA@AZ31B, f) polyOFPA@AZ31B and h) polyPFPA/polyOFPA @AZ31B.

Table S5. Fitted electrochemical parameters of the EIS of AZ31B Mg alloy with different coatings and different immersion corrosion times.

Specimen	R_s (Ω cm^2)	CPE_f (Ω^{-1} s^{-n} cm^{-2})	n	R_f (Ω cm^2)	CPE_{dl} (Ω^{-1} s^{-n} cm^{-2})	n	R_{ct} (Ω cm^2)	R_L (Ω cm^2)	L (H/cm^2)	R_P (Ω cm^2)
0 d										
Bare AZ31B	4.1				5.49×10^{-5}	0.88	5.48×10^{2}	7.72×10^{2}	1.34×10^{3}	3.21×10^{2}
polyPFPA/ polyOFPA	252	9.90×10^{-10}	0.97	6.25×10^{10}						6.25×10^{10}
polyPFPA	263	1.39×10^{-9}	0.95	3.33×10^{7}	5.17×10^{-9}	0.54	9.85×10^{7}			1.32×10^{8}
polyOFPA	383	1.16×10^{-9}	0.97	2.11×10^{8}	4.76×10^{-9}	0.57	5.46×10^{8}			7.57×10^{8}
1 d										
Bare AZ31B	4.2				5.14×10^{-5}	0.88	6.97×10^{2}	6.23×10^{2}	6.05×10^{3}	3.29×10^{2}
polyPFPA/ polyOFPA	253	9.98×10^{-10}	0.97	5.91×10^{10}						5.91×10^{10}
polyPFPA	180	1.20×10^{-9}	0.96	1.39×10^{6}	4.10×10^{-8}	0.72	1.22×10^{7}			1.36×10^{7}
polyOFPA	377	1.18×10^{-9}	0.97	9.35×10^{7}	6.32×10^{-9}	0.68	1.81×10^{8}			2.75×10^{8}
3 d										
Bare AZ31B	4.4				5.22×10^{-5}	0.88	8.32×10^{2}	7.53×10^{2}	4.87×10^{3}	3.95×10^{2}
polyPFPA/ polyOFPA	229	9.80×10^{-10}	0.98	9.28×10^{10}						9.28×10^{10}
polyPFPA	438	3.53×10^{-9}	0.89	7.51×10^{3}	2.38×10^{-6}	0.68	4.05×10^{4}			4.80×10^{4}
polyOFPA	287	2.44×10^{-7}	0.81	2.87×10^{5}	8.98×10^{-10}	0.99	4.15×10^{3}			2.91×10^{5}
7 d										
Bare AZ31B	4.6				4.93×10^{-5}	0.88	1.01×10^{3}	7.36×10^{2}	6.70×10^{3}	4.26×10^{2}
polyPFPA/ polyOFPA	268	1.01×10^{-9}	0.97	5.28×10^{10}						5.28×10^{10}
polyPFPA	450				9.28×10^{-6}	0.63	8.70×10^{3}	1.36×10^{4}	7.76×10^{3}	5.31×10^{3}
polyOFPA	470	6.74×10^{-7}	0.84	1.35×10^{5}	1.38×10^{-7}	0.82	7.94×10^{2}			1.35×10^{5}
14 d										
Bare AZ31B	5.0				6.30×10^{-5}	0.84	1.01×10^{3}	6.92×10^{2}	3.14×10^{3}	4.11×10^{2}
polyPFPA/ polyOFPA	219	9.06×10^{-10}	0.98	2.09×10^{11}						2.09×10^{11}
polyPFPA	457				9.82×10^{-6}	0.73	2.95×10^{3}	3.97×10^{3}	4.24×10^{3}	1.69×10^{3}
polyOFPA	447	7.46×10^{-7}	0.84	5.96×10^{4}	1.83×10^{-7}	0.84	2.88×10^{2}			5.99×10^{4}

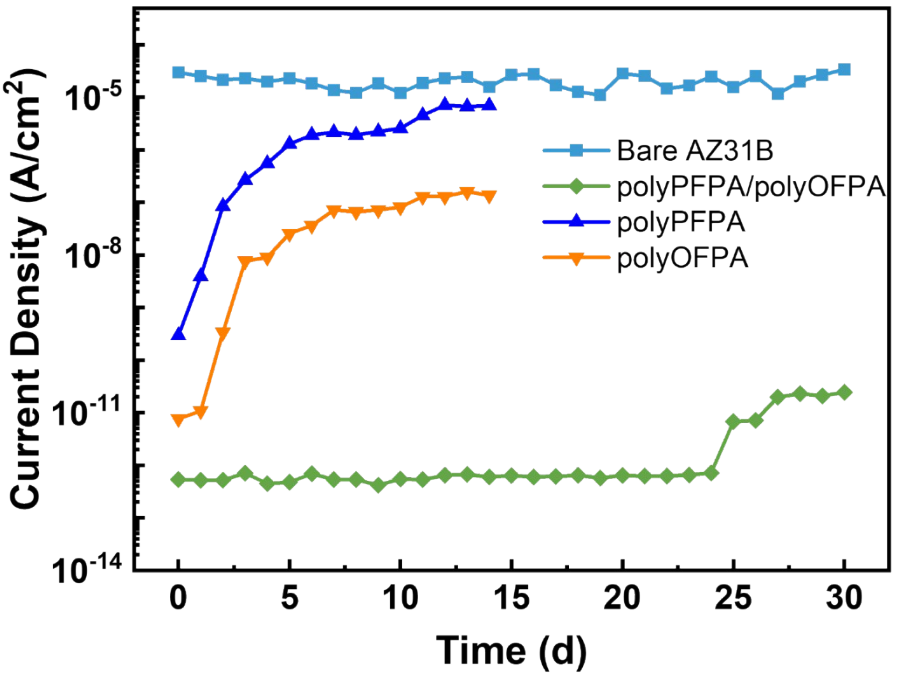

Figure S18. Comparison of the change of corrosion current density derived from linear polarization curve over one month for different coatings. As can be seen, Janus polyPFPA/polyOFPA have shown best defense against corrosion on AZ31B.

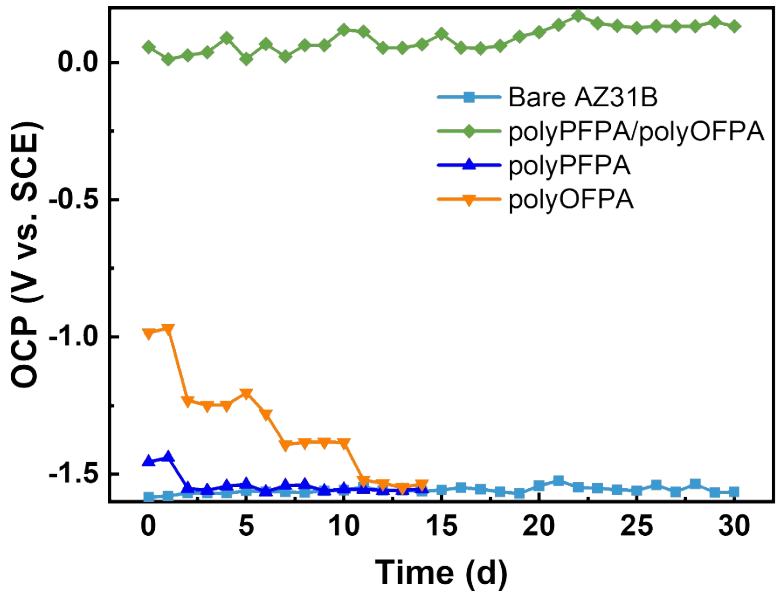

Figure S19. Open circuit potential (OCP) stability of different layers over a month. As can be seen, Janus polyPFPA/polyOFPA have shown superior defense against corrosion on AZ31B, as the steadfast open circuit potential (OCP) near 0 V and was kept over one month.

Table S6. Fitted electrochemical parameters of the polarization curves of AZ31B Mg alloy with different coatings after 14 days of immersion.

Specimen	E_{corr} (V vs. SCE)	b_a (mV/dec)	b_c (mV/dec)	B (mV/dec)	i_{corr} (A/cm^2)	Corrosion rate (mm/y)
Bare AZ31B	-1.41	252	136	38	1.06×10^{-6}	2.39×10^{-2}
polyPFPA/ polyOFPA	-0.10	246	157	42	2.86×10^{-13}	6.45×10^{-9}
polyPFPA	-1.40	253	141	39	3.12×10^{-7}	7.04×10^{-3}
polyOFPA	-1.38	259	145	40	4.59×10^{-8}	1.04×10^{-3}

4.2 AZ31B protected from different coatings through neutral salt spray test

The uncoated AZ31B alloy suffered significant corrosion, as evidenced by the SEM images, which showed a heavy buildup of corrosion products and EDS mapping revealed high levels of oxygen and chlorine indicative of corrosion activity (Figure S20). Conversely, the double-layered polyPFPA/polyOFPA@AZ31B showcased remarkable efficacy in corrosion inhibition, maintaining an intact surface morphology and uniform elemental distribution, implying the formation of a protective fluorine-containing barrier (Figure S21a, b). The polyPFPA@AZ31B, while offering some protection, however, due to limited repellency to water, corrosion medium, i.e., Na^+ and Cl^- finally infiltrate into the inner space and adhere to the surface, forming microcrystals and leading to breakage of AZ31B, as revealed by SEM and EDX images in Figure S21c, d. As for polyOFPA@AZ31B, liquid can permeate along the cracks at the interface due to poor adhesion to substrate, can obvious cracks can be seen located at the surface of AZ31B Figure S21e, f. The superior performance of the polyPFPA/polyOFPA coating can be attributed to a dual-layer mechanism where the polyOFPA layer serves as a primary barrier, firmly adhering the coating to the substrate surface, enhancing the overall strength of the coating, and preventing lateral spreading of corrosive agents within the coating, and the polyPFPA layer further reinforces protection by efficiently blocking the penetration of corrosive media, as revealed in **Figure 4**. This combination not only preserves the surface of the alloys but also suggests a promising strategy for advanced material applications requiring high corrosion resistance.

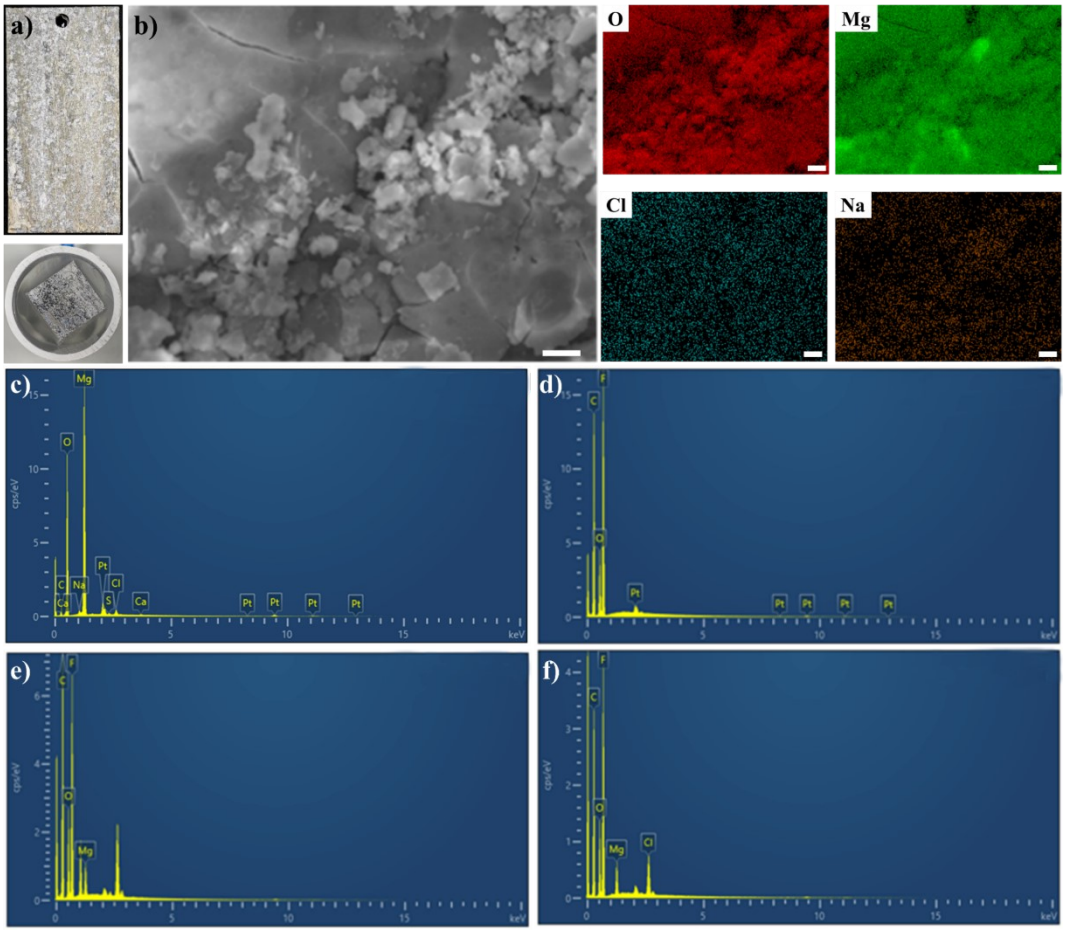

Figure S20. Morphology changes of bare AZ31B after salt spray test. a) Digital graph and b) SEM image and corresponding EDX mapping image with tested element as O, Mg, Na and Cl. Element contents distribution in EDX mapping of c) bare AZ31B, d) polyPFPA/polyOFPA@AZ31B, e) polyPFPA@AZ31B and f) polyOFPA@AZ31B.

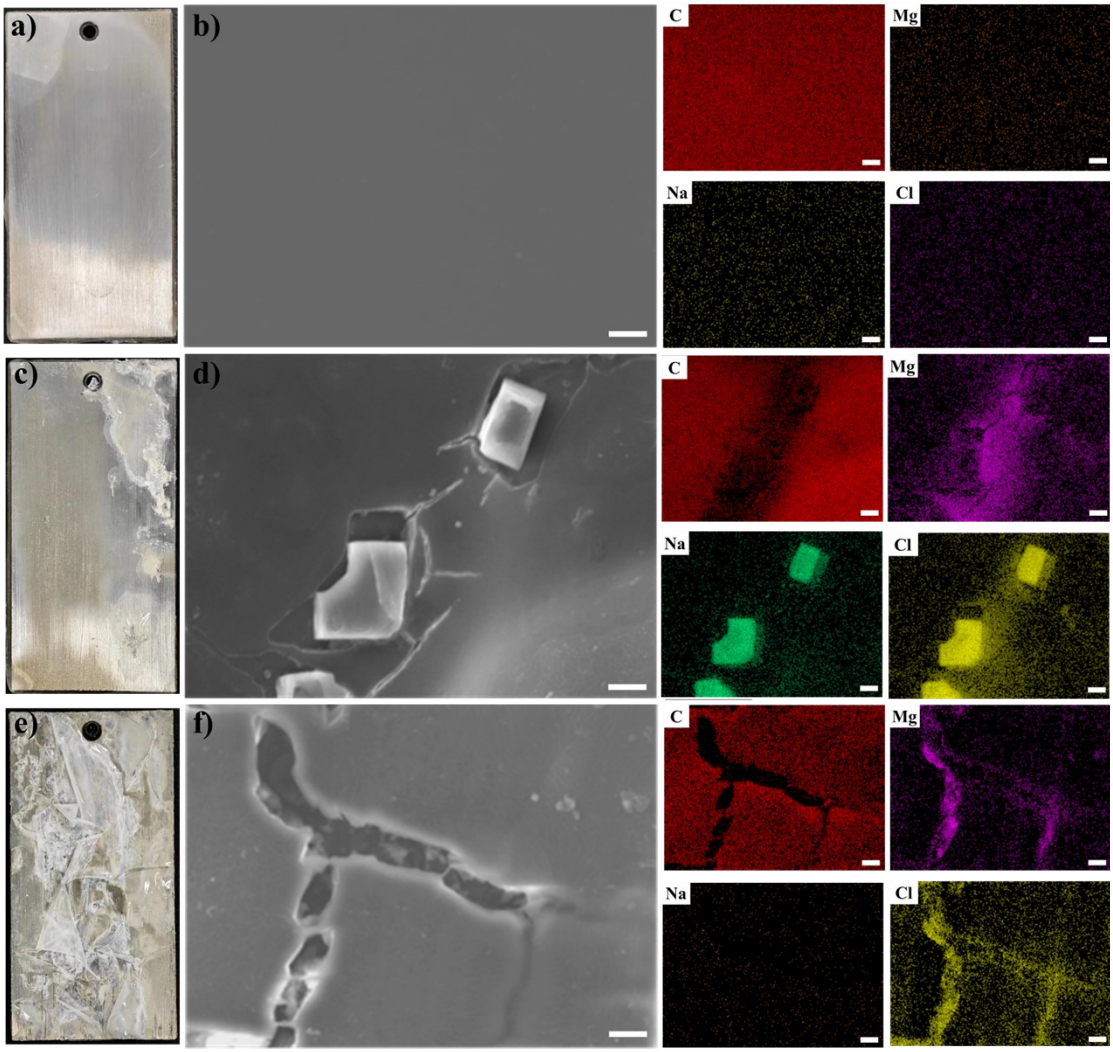

Figure S21. Digital graph and SEM image and corresponding EDX mapping image with tested element as C, Mg, Na and Cl in the neutral salt spray test. The scale bar is 10 μm. a, b) polyPFPA/polyOFPA@AZ31B; c, d) polyPFPA@AZ31B and e, f) polyOFPA@AZ31B.

4.3 Anti-corrosion performances of different coatings when immersed in 3.5% NaCl solution

In addition, further tests were conducted by immersing all the samples in 3.5% NaCl solution to examine the anti-corrosion performance. Similar trend can be seen as those presented in 3.5% NaCl solution (Figure S22), providing further evidence to the superior anti-corrosion effect of our composite coatings here. That is to say, the polyPFPA/polyOFPA coating can serve as a formidable barrier against corrosion processes (Figure S22b). In contrast, as for the polyPFPA@AZ31B and polyOFPA@AZ31B, obvious cracks can be seen located at the surface of AZ31B (Figure S22c, d).

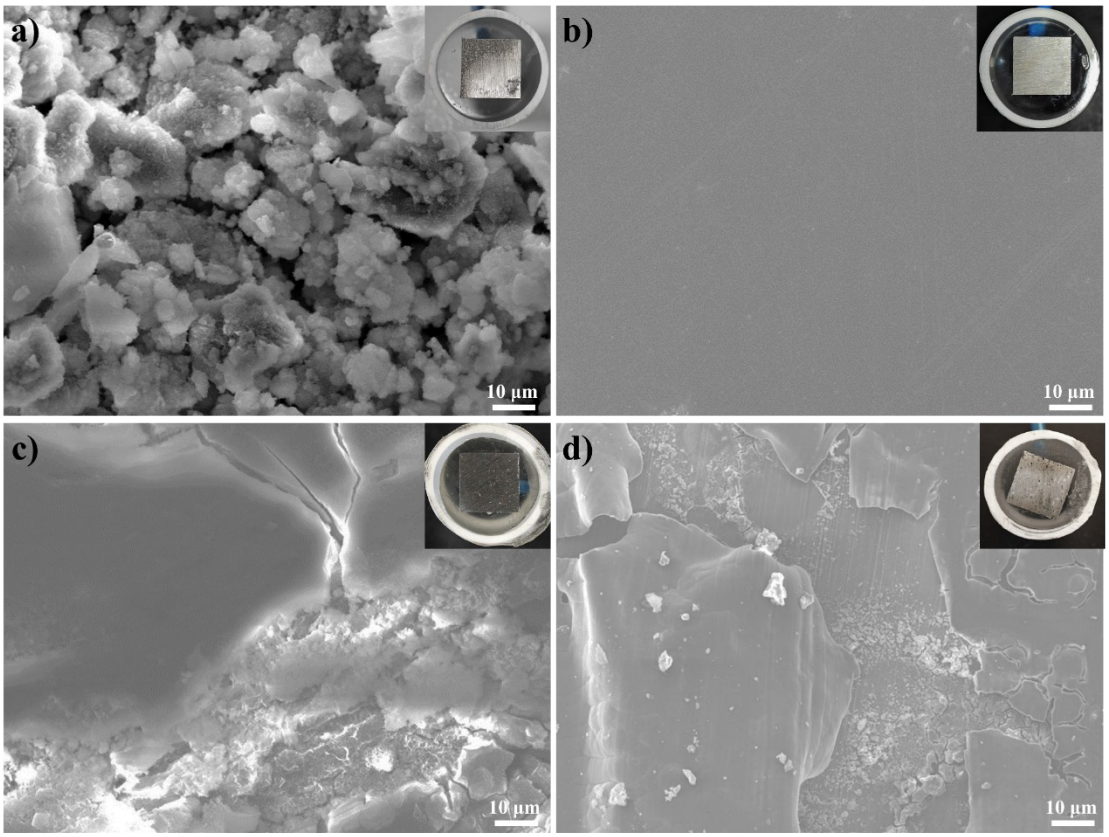

Figure S22. Morphology changes of AZ31B covered with different coatings after immersed in 3.5% NaCl solution for 14 days. SEM image of a) bare AZ31B,b) polyPFPA/polyOFPA@AZ31B, c) polyPFPA @AZ31B and d) polyOFPA@AZ31B. The inset is the corresponding digital graphs.

4.4 In-situ scanning vibration electrode (SVET) measurements

The in-situ scanning vibration electrode (SVET) measurements was further performed, offering a comprehensive evaluation of the anti-corrosive behavior of polyPFPA, poly OFPA, and the combined poly PFPA/polyOFPA coatings over a critical period of 72 hours. In the initial stages at 1 hour, the polyPFPA/polyOFPA coating maintains a low and uniform current density, as depicted by the almost flat 3D topography and the consistent 2D contour patterns. This stability points to an effective protect effect, likely due to the creation of a robust protective film that precludes the penetration of corrosive elements. As time progresses, the hybrid polyPFPA/polyOFPA coatings still exhibits a synergy that enhances barrier robustness, as seen by the minimal fluctuation in current density, even after 72 hours, underscoring its sustained protective efficacy (Figure 23a-c). The persistent low current density and the absence of peaks in the 3D plot and 2D map for the polyPFPA/polyOFPA coating indicate that the dual-layer system effectively mitigates the electrochemical reactions that lead to corrosion. In stark contrast, the polyPFPA coating undergoes a marked escalation in ionic current density, especially beyond the 24-hour mark (Figure 23e). This is visually captured in the 3D representations, transitioning from a smooth profile to a topographically varied one, and corroborated by 2D contour maps that evolve from tranquil blues to alarming reds, signaling the onset and proliferation of active corrosion sites. The escalating terrain in the 3D SVET plots and the intensifying red zones in the 2D maps collectively indicate a progressive deterioration of the protective capabilities, culminating in pronounced corrosion activity at 72 hours (Figure 23f). Conversely, the polyOFPA

coating, while showing an increase in activity, does not reach the intensity of the polyPFPA, suggesting intermediate protective efficacy(Figure 23g-i). The superior performance of the polyPFPA/polyOFPA coating is likely attributable to the synergistic interplay between PFPA's adhesive characteristics and OFPA's hydrophobic nature, resulting in a composite layer that imparts enhanced protection.

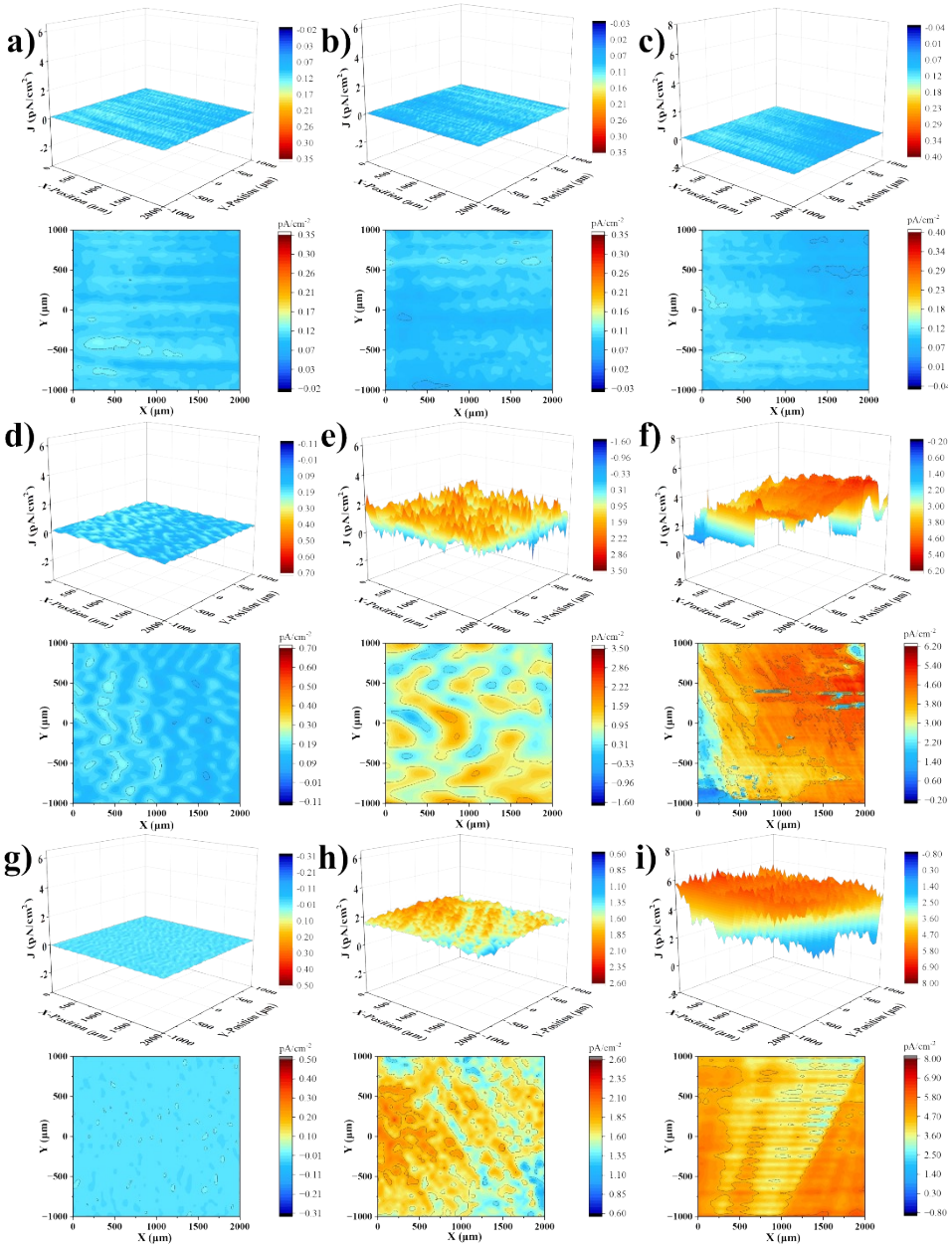

Figure S23. SVET 3D current density plots and 2D contour maps for a-c) polyPFPA/polyOFPA, d-f) polyPFPA and g-i) polyOFPA coatings at 1 h, 24 h, and 72 h time intervals.

4.5 Anti-corrosion performances of different coatings on Q235 mild steel and H62 brass

Finally, the exceptional adhesion properties of our composite coatings extend their utility beyond magnesium alloys, proving to be highly effective as protective layer for carbon structural steel (Q235) and brass (H62) as well, thereby demonstrating their remarkable versatility and broad-spectrum anti-corrosion performance across diverse metallic substrates (Figure S24-S26). After the salt spray test, the surface of bare Q235 and H62 samples showed obvious corrosion characteristics, while the samples coated with polyPFPA/polyOFPA coating remained smooth and flat (Figure S24). This indicates the remarkable corrosion resistance of polyPFPA/polyOFPA coating.

Furthermore, the potentiodynamic polarization curves (Figure S25a and S26a) clearly show that the double-layered polyPFPA/polyOFPA coating dramatically reduces the I_{corr} to 2.78×10^{-13} A/cm^2 for Q235 and 3.12×10^{-13} A/cm^2 for H62. This drastic reduction indicates an exceptional decrease in the rate of corrosion, highlighting the effectiveness of the polyPFPA/polyOFPA in protecting different substrates. In addition, the OCP offers insights into the stability of the coating in an electrolyte. The metals with polyPFPA/polyOFPA coatings show more positive OCP values (Figure S25b and S26b), suggesting a more noble character and further reinforcing its enhanced corrosion resistance. EIS Nyquist plots (Figure S25c and S26c) further substantiate the corrosion resistance of the double-layered coating, revealing an extremely high R_p value of 8.24×10^{10} Ω cm^2 for Q235 with polyPFPA/polyOFPA coating. Those values are orders of magnitude greater than those for single-layered coatings (Q235) and bare

substrates, reflecting its strong barrier properties and ability to impede the electrochemical processes that lead to corrosion. The Bode plots (Figure S25d and S26d) display a similar trend, where the polyPFPA/polyOFPA coating shows a significantly higher impedance modulus |Z| at 0.01 Hz compared to single-layered coatings (Q235) and bare substrates, indicating a more robust and protective layer. Additionally, the EIS plots exhibit a extended capacitive behavior for polyPFPA/polyOFPA, which suggests that the interface forms a more uniform and defect-free layer, contributing to its enhanced protective characteristics. In conclusion, the polyPFPA/polyOFPA double-layered coating demonstrates outstanding anti-corrosion properties on Q235 steel and H62 brass. The data indicate a remarkable synergy between the polyPFPA and polyOFPA layers owning to the highly covanlently connected structures, resulting in a composite coating showing excellent anti-corrosion performances in terms of corrosion current density, polarization resistance, and impedance modulus. This comprehensive analysis underscores the potential of the polyPFPA/polyOFPA coating system as a highly effective method for corrosion protection in industrial applications.

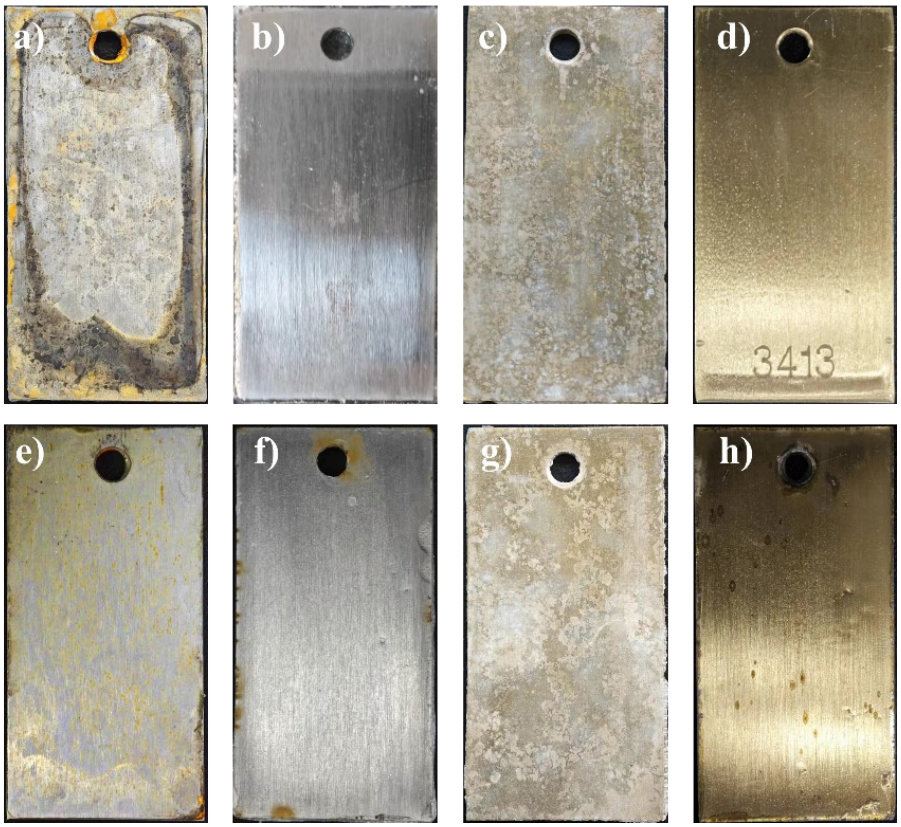

Figure S24. Morphology of uncoated and coated Q235 and H62 after one-year equivalent neutral salt spray test: a,e) bare Q235, b, f) polyPFPA/polyOFPA@Q235, c, g) bare H62, d, h) polyPFPA/polyOFPA@H62.

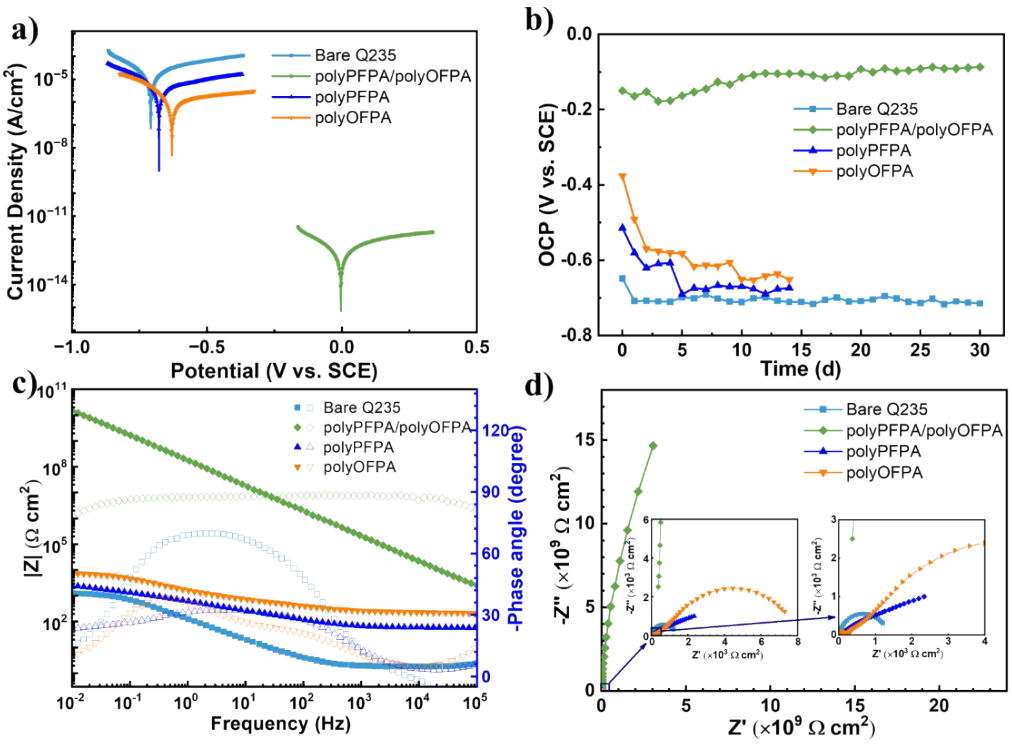

Figure S25. Electrochemical analysis and stability characterization of Q235 mild steel with different coatings: a) Potentiodynamic polarization curves for 14 days, b) Open circuit potential (OCP) stability over a month, c) Bode plots and d) Nyquist plots (impedance modulus and phase angle across frequencies) for 14 days. Each plot compares the performance of bare Q235, Q235 with polyPFPA/polyOFPA, polyPFPA, and polyOFPA coatings during immersion tests.

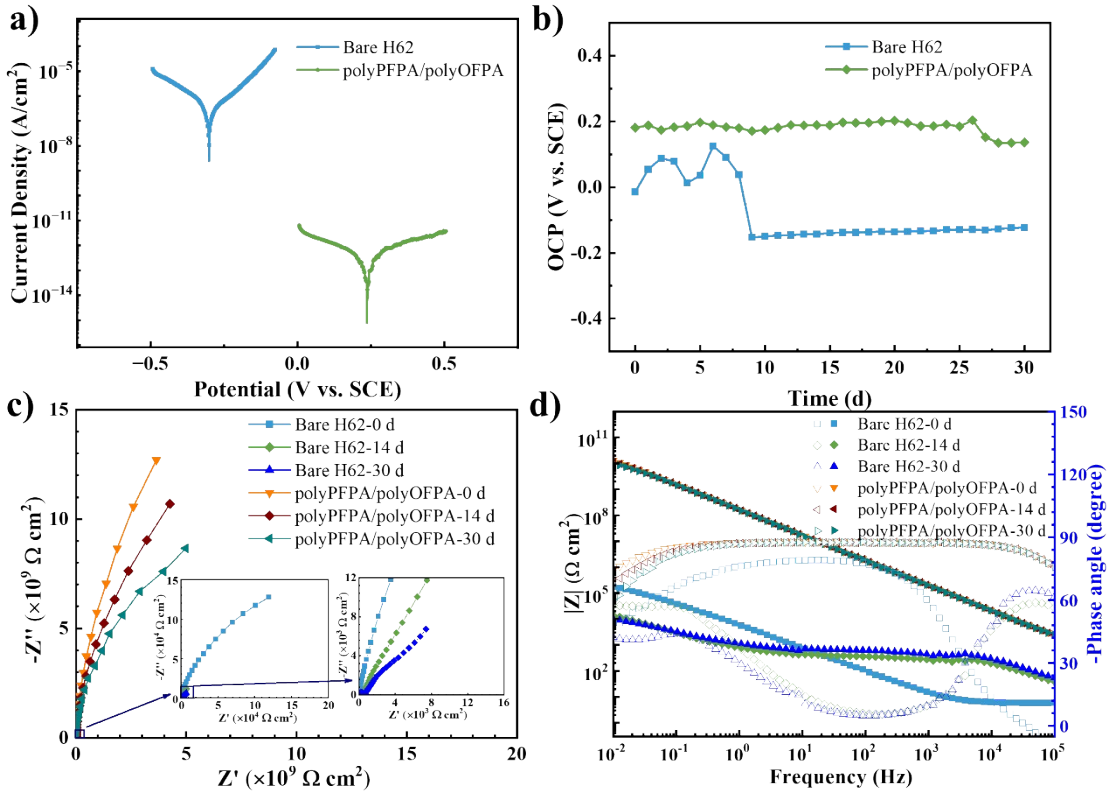

Figure S26. Electrochemical analysis and stability characterization of H62 brass with different coatings: a) Potentiodynamic polarization curves for 14 days, b) Open circuit potential (OCP) stability over a month, c) Nyquist plots and d) Bode plots (impedance modulus and phase angle across frequencies) for 0 day 14 days and 30 days. Each plot compares the performance of bare H62 and polyPFPA/polyOFPA@H62 during immersion tests.

Supporting references

(1) Liu S.; Li T.; Li R.; Qi K.; Liu Z., A comparative study of microstructure and corrosion resistance in DP980 steel joints under different laser welding method, *J. Mater. Res. Technol.* **2023**, *27*, 3870-3880.

(2) Poursaee A., Potentiostatic transient technique, a simple approach to estimate the corrosion current density and Stern–Geary constant of reinforcing steel in concrete, *Cem. Concr. Res.* **2010**, *40*(9), 1451-1458.

(3) Mukherjee R.; Badaik S.; Pandey A.; K.; et al. A hybrid coating of organometallic complex with a silane coupling compound to protect galvannealed (GA) steel from white rust without sacrificing weldability, *Mater. Chem. and Phys.* **2023**, *309*, 128292.

(4) Aghili M.; Yazdi M. K.; Ranjbar Z.; et al, Anticorrosion performance of electro-deposited epoxy/amine functionalized graphene oxide nanocomposite coatings, *Corros. Sci.*, **2021**, *179*, 109143.

(5) Prabhu D.; Padmalatha R., Corrosion inhibition of 6063 aluminum alloy by Coriandrum sativum L seed extract in phosphoric acid medium, *J. Mater. Environ. Sci.* **2013**, *4*, 732-743.